N. Hosseini, M. Tadjfar, M. Saeedi, A. Abbà
Large-Eddy Simulation of Vortex Interaction in Pitching-Fixed Tandem Airfoils
Physics of Fluids, Vol. 36, N. 8, 2024, 085132 (18 pages)
doi:10.1063/5.0218556

Large-eddy simulation of vortex interaction in pitching-fixed tandem airfoils

Niloofar Hosseini (نیلوفر حسینی) [1,a], Mehran Tadjfar (مهران تاج فر) [1], Mohammad Saeedi (محمد سعیدی) [2], Antonella Abbà [3]

[1] Turbulence and Multi-Phase Flow Laboratory, Aerospace Engineering Department, Amirkabir University of Technology, Tehran, Iran

[2] Department of Mechanical Engineering, Dalhousie University, Halifax, NS, Canada

[3] Dipartimento di Scienze e Tecnologie Aerospaziali, Politecnico di Milano, Via La Masa 34, 20156 Milano, Italy

ABSTRACT

In this study, the interaction of vortices generated from an oscillating airfoil with a hindfoil placed downstream of the oscillating forefoil at low-Reynolds-number flow was investigated numerically. The forefoil entered a deep dynamic stall induced by large-amplitude pitching oscillation. The dynamic stall process is characterized by unsteady separation and the formation of a strong clockwise vortex. A wall-resolved large-eddy simulation approach was applied to compute the flowfield. The numerical measurements were performed for an incompressible flow at a Reynolds number of Re=30,000 based on chord length with a pitching reduced frequency of K=0.5, and amplitude of A=14.1° over Selig-Donovan7003 airfoils. A single-airfoil case was validated against numerical and experimental measurements. In the present study, we investigated the flowfield and aerodynamic coefficients resulting from the deep dynamic stall of the pitching forefoil and the vortex interaction in tandem-airfoil configuration related to micro air vehicle applications by employing large-eddy simulation approach. Large-eddy simulation was also compared to two-dimensional unsteady Reynolds-averaged Navier-Stokes simulation to determine the accuracy and validity of the low-fidelity approach in prediction of deep dynamic stall and vortex interaction at low-Reynolds-number flow.

KEYWORDS: Tandem airfoils, Pitching motion, Dynamic stall, Low-Reynolds-number flows, URANS, LES.

NOMENCLATURE

a	Forefoil angle of attack
a_0	Mean forefoil angle of attack [=8°]
A	Pitching motion amplitude
C	Chord length [=0.12 m]

[a] Corresponding author.
Email address: niloofarhosseini@aut.ac.ir (Niloofar Hosseini)

C_d	Drag force coefficient
C_f	Skin friction coefficient
C_l	Lift force coefficient
C_p	Pressure coefficient
D	Drag force
f	Pitching frequency
h	Vertical spacing between two airfoils
k	Turbulent kinetic energy
K	Pitching reduced frequency [=0.5]
l	Horizontal spacing between two airfoils
L	Lift force
L/D	Aerodynamic performance
$\bar{p}$	Filtered pressure
Re	Reynolds number based on chord length
s	Span width
S	Strain rate tensor
T	Pitching time cycle
$\bar{u}_i$	Filtered velocity
$u_i'u_j'$	Reynolds stress tensor
U_∞	Free stream velocity [=3.77 m/sec]
Δ	Grid-level filter width
ν	Kinematic viscosity
τ_{ij}	SGS stress tensor
τ^*_{ij}	Deviatoric form of the SGS stress tensor
ω	Vorticity
Ω	Rotation tensor

1. INTRODUCTION

Many applications involve oscillating airfoils, including micro air vehicles (MAVs) and unmanned aerial vehicles (UAVs). The oscillation can be pure pitch, pure plunge, or a combined motion. Aerodynamic

characteristics of an oscillating airfoil, including lift, drag, aerodynamic performance (L/D), and stall behavior depend on different parameters such as effective angle of attack, reduced frequency of oscillation, or Reynolds number. The effects of different parameters on the aerodynamic characteristics of oscillating airfoils have been investigated by many researchers. Fenercioglu and Centiner [1] performed an experimental study on a Selig-Donovan7003 (SD7003) oscillating airfoil with combined pitch and plunge motion over a wide range of reduced frequencies. They stated that the categorization of vortex formation was independent of the Reynolds number. However, it was strongly dependent on the reduced frequency. Liang et al. [2] observed that the vortex shedding pattern of a plunging airfoil becomes asymmetric at sufficiently high frequencies. The degree of this asymmetry increases with the Reynolds number. Thakor et al. [3] investigated the effect of amplitude, reduced frequency, Reynolds number, and asymmetry parameter for a two-dimensional asymmetrically pitching airfoil. They stated that reduced frequency and asymmetry parameter significantly influenced the vortex structure in the wake. Lu et al. [4] numerically investigated the effects of amplitude and nonsinusoidal motion on thrust generation of a pitching airfoil. They observed that higher thrust was produced in cases of large-amplitudes, although thrust production slowed beyond a certain amplitude. Han et al. [5] studied the flowfield over a three-dimensional (3-D) flapping wing at different Reynolds numbers. They reported that the propulsive performance of the flapping motion highly depends on the kinematic parameters. Some researchers have focused on the kinematic equivalence between pitch and plunge motions. Sarkar [6] stated that equivalent pitch closely matched plunge motion in terms of flowfield and load, even at high amplitudes.

Oscillating motion may lead to unsteady flow and dynamic stall conditions. Dynamic stall may involve the shedding of large vortices from the trailing-edge of the airfoil. These vortices can influence the aerodynamic behavior of the airfoil. So, studying the dynamic stall phenomenon is crucial in understanding the aerodynamic performance of flapping wings. Visbal [7] performed a large-eddy simulation (LES) study on the dynamic stall behavior of an SD7003 airfoil with plunging motion at low Reynolds numbers ($Re < 60{,}000$) for different amplitudes and frequencies. Guillaud et al. [8] performed large-eddy simulations on a pitching airfoil to examine the effect of reduced frequency on the dynamic stall phenomenon at a Reynolds number of 20,000. They stated that as the reduced frequency increased, the leading-edge vortex (LEV) appeared at higher angles of attack, and its lifetime decreased. Ashraf et al. [9] studied the effect of plunging amplitude at different reduced frequencies in a plunging airfoil using 2-D (two-dimensional) and 3-D Navier-Stokes simulations at Re=20,000. As the oscillation amplitude increased, the flow transitioned from periodic to chaotic behaviors in the 2-D analysis for a given frequency. 3-D simulations confirmed this phenomenon. 3-D simulations also showed that at low frequencies and large amplitudes, the LEV remained stable, while in the opposite condition, the LEV broke into small structures. Yu et al. [10] showed experimentally that the stall angle was delayed as reduced frequency increased for a pitching airfoil at Re=4500. Some research focused on different strategies to control dynamic stall to improve aerodynamic performance and stability of the airfoil. Zhu et al. [11] used a passive vortex generator. Active flow control methods, including plasma actuators [12] or synthetic jet actuators [13] have also been used.

Tandem flapping airfoils inspired by natural flyers in aerial vehicles offer several advantages, including enhanced flight capabilities, energy efficiency, and maneuverability. These points have motivated researchers to study tandem flapping airfoils for creating efficient MAVs and UAVs at low-Reynolds-number regimes. Tay et al. [14] investigated the effect of adding a tail behind single or biplane flapping airfoils. They evaluated the effects of the relative positioning of the airfoils on efficiency and average thrust and lift coefficients. Results showed that the total lift of the case with a single upstream flapping airfoil was much higher than the combined lift coefficient of two separate airfoils (flapping plus static). Wu et al. [15] studied a tandem flapping-fixed airfoil configuration and investigated the effects of horizontal spacing, vertical spacing, and the angle of attack of the fixed airfoil on thrust and lift coefficients. Compared to a

fixed airfoil, the studied configuration demonstrated improved aerodynamic performance. Meng et al. [16] studied the flowfield of three flapping wings at a low Reynolds number. They investigated the effect of the spatial arrangement of the wings with 3-D simulations. They found that the lift of the entire wings decreased with an increase in the number of wings. Jurado et al. [17] analyzed the effect of aspect ratio on the aerodynamic performance of two flapping wings in tandem configuration through direct numerical simulation at Re=1000. The aerodynamic performance of the hindwing was affected by the vortices shed by the forewing. However, the forewing was not affected by the hindwing. The vortex interaction of two flapping airfoils in tandem configuration was also investigated by Xu et al. [18]. They stated that the propulsive performance of airfoils is highly dependent on longitudinal distances and phase differences. Broering and Lian [19] performed a 2-D numerical investigation on two flapping wings in tandem. They studied the effect of horizontal spacing and phase angle and stated that these parameters are effective in the timing of vortex interaction between the airfoils. They also observed that changing the phase angle had a similar effect as changing the spacing. Chen et al. [20] analyzed a tandem configuration with plunging and asymmetric pitching. They examined the effects of mean angle of attack, phase angle, and horizontal spacing between the airfoils. Hosseini et al. [21] performed optimization studies on tandem-airfoil configurations to achieve a higher lift-to-drag ratio. They studied a pitching-fixed airfoil configuration and investigated the effects of horizontal spacing, vertical spacing, and the angle of attack of the fixed airfoil on the aerodynamic performance of the airfoils by implementing machine learning and optimization techniques. In another optimization study with the same tandem configuration [13], they used synthetic jets on each airfoil to control dynamic stall and improve the aerodynamic performance of the tandem configuration. Ji et al. [22] also conducted an optimization study on tandem flapping wings for optimal performance in terms of thrust and efficiency.

Previous studies on tandem-airfoil configurations mainly focused on investigating tandem flapping wings, with fewer researchers examining the interaction between a pure pitching wing and a fixed wing in tandem configuration at low Reynolds numbers. Moreover, large-eddy simulation of the pitching-fixed airfoil arrangement with deep dynamic stall was conducted in this study. Studying tandem-airfoils with dynamic stall using large-eddy simulations provides a more realistic representation of flow features, including vortex shedding, vortex interaction, and dynamic stall onset. This approach leads to improved insights into flow aerodynamic performance and stall characteristics of tandem configuration.

In the current study, the vortex interaction of a tandem-airfoil configuration, which consists of an oscillating forefoil and a stationary hindfoil, was investigated by large-eddy simulation. The forefoil oscillated with pure-pitch motion, while the hindfoil remained fixed. Following a previous study conducted by the authors [21], an optimal geometrical configuration of two SD7003 airfoils in tandem configuration was found at Re=30,000, using optimization techniques and machine learning through two-dimensional unsteady Reynolds-averaged Navier-Stokes (URANS) simulations. In the present work, we used the same optimal configuration obtained in the study [21] using LES approach. In the present study, we aim to analyze the vortex interaction and the aerodynamic characteristics in tandem airfoils with pitching motion by large-eddy simulation. This study involves three-dimensional LES simulation, despite the flow being inherently two-dimensional. LES was additionally employed to assess the accuracy of two-dimensional URANS simulations. Dynamic stall and the vortex interaction in the considered configuration were compared to 2-D URANS simulation to examine the reliability of low-fidelity solvers for predicting largely separated flows.

The novelty of this study lies in the investigation of a pitching-fixed configuration under dynamic stall conditions at such low Reynolds numbers. This investigation has not been extensively covered in the literature. Additionally, LES was employed to capture the three-dimensional aspects of flow that are often

overlooked in two-dimensional analyses. This approach offers practical insights for the development of more efficient aerodynamic systems. By comparing LES results with URANS simulation, this research bridges the gap between high-fidelity and low-fidelity modeling techniques, potentially leading to more accurate and efficient design methodologies for MAVs and other aerodynamic applications with tandem configurations.

A particular operating condition corresponding to a Reynolds number of 30,000, a reduced frequency of 0.5, and an effective angle of attack ranging from -6.1 to 22.1 degrees was selected. This flow condition was chosen because of its relevance for MAV applications.

2. SIMULATION SETUP

2.1. Tandem configuration specifications

In this study, two airfoils were placed in a tandem configuration. An asymmetric Selig-Donovan7003 (SD7003) airfoil was selected for both airfoils. This airfoil demonstrates relatively high performance at low (transitional) Reynolds numbers. There is also substantial database available in the open literature for this airfoil. The forefoil moved with a pure-pitch motion, while the hindfoil remained stationary at a fixed angle of attack. An optimal geometrical configuration obtained from an optimization study was considered in this paper. In our previous study [21], we optimized the vertical and horizontal spacings between the airfoils and the angle of attack of the hindfoil to maximize the aerodynamic performance of tandem airfoils, defined as the total lift coefficient to the total drag coefficient (L/D). The horizontal and vertical spacings between the airfoils were fixed at l=2.62C and h=0.44C, respectively, defined between the quarter-chord point of the forefoil and the three-quarter-chord point of the hindfoil. The angle of attack of the hindfoil was set to α=7.216° (see Fig. 1).

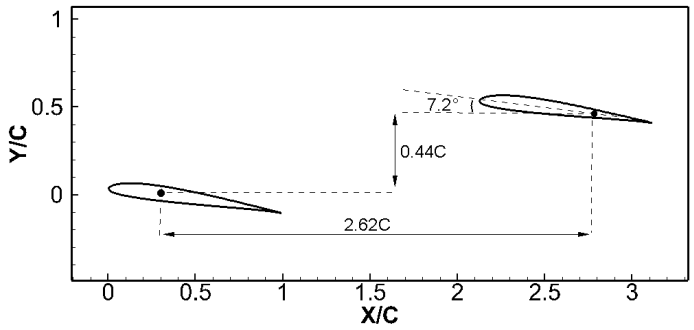

Fig. 1. Schematic of tandem configuration representing vertical and horizontal spacings between the airfoils and the angle of attack of the hindfoil.

The forefoil had a sinusoidal pitching motion about its quarter-chord point:

$$a = a_0 + \mathrm{Asin}(2\pi \mathrm{ft}) \quad (1)$$

Where a_0=8˚ is the mean angle of attack, f=5 is the pitching frequency, and A=14.1˚ is the pitching amplitude. These parameters correspond to the angle of attack range of -6.1˚≤ a ≤ 22.1˚. Reduced frequency of pitching motion was defined as Eq. (2).

$$\mathrm{K} = \frac{\pi \mathrm{fC}}{\mathrm{U}_\infty} = 0.5 \quad (2)$$

Where C represents the airfoil chord length and U_∞ the free-stream velocity. According to f=5, the oscillation time cycle of the pitching motion is equal to T=0.2.

2.2 Governing equations and flow solver

Three-dimensional incompressible implicitly filtered Navier-Stokes equations were solved. The equations are described in Eq. (3) and Eq. (4).

$$\frac{\partial \bar{\mathrm{u}}_\mathrm{i}}{\partial \mathrm{x}_\mathrm{i}} = 0 \quad (3)$$

$$\frac{\partial \bar{\mathrm{u}}_\mathrm{i}}{\partial \mathrm{t}} + \frac{\partial}{\partial \mathrm{x}_\mathrm{j}}\left(\bar{\mathrm{u}}_\mathrm{i}\bar{\mathrm{u}}_\mathrm{j}\right) = -\frac{1}{\rho}\frac{\partial \bar{\mathrm{p}}}{\partial \mathrm{x}_\mathrm{i}} + \nu \frac{\partial^2 \bar{\mathrm{u}}_\mathrm{i}}{\partial \mathrm{x}_\mathrm{j}\,\partial \mathrm{x}_\mathrm{j}} - \frac{\partial \tau_{\mathrm{ij}}}{\partial \mathrm{x}_\mathrm{j}} \quad (4)$$

Where $\bar{\mathrm{u}}_\mathrm{i}$ and $\bar{\mathrm{p}}$ represent the filtered velocity and pressure, respectively, and τ_{ij} is the so-called subgrid-scale (SGS) stress tensor. The SGS stress tensor appeared in the above system of governing equations as the result of the filtering process and is defined as Eq. (5).

$$\tau_{\mathrm{ij}} = \overline{\mathrm{u}_\mathrm{i}\mathrm{u}_\mathrm{j}} - \bar{\mathrm{u}}_\mathrm{i}\bar{\mathrm{u}}_\mathrm{j} \quad (5)$$

To close the above system of governing equations, an SGS model was needed to model the deviatoric form of the SGS stress tensor (τ^*_{ij}).

$$\tau^*_{\mathrm{ij}} = \tau_{\mathrm{ij}} - \frac{1}{3}\tau_{\mathrm{kk}}\delta_{\mathrm{ij}} = -2\,\nu_{\mathrm{SGS}}\bar{\mathrm{S}}_{\mathrm{ij}} \quad (6)$$

Where $\bar{\mathrm{S}}_{\mathrm{ij}}$ is the filtered resolved strain rate tensor and ν_{SGS} is the subgrid-scale kinematic viscosity. ν_{SGS} was determined from the flowfield variables using the dynamic Smagorinsky SGS model as Eq. (7).

$$\nu_{\mathrm{SGS}} = \mathrm{C_s}\Delta^2|\bar{\mathrm{S}}| \quad (7)$$

Where Δ is the grid-level filter width and $\mathrm{C_s}$ is the model coefficient and is dynamically calculated through the procedure proposed by Lilly [23].

The equations were solved using the open-source finite-volume computational fluid dynamics (CFD) package OpenFOAM. The simulations were in transient mode with a second-order implicit backward temporal scheme. The spatial terms were discretized with a second-order central scheme due to its minimum numerical dissipation. Pressure-velocity coupling was performed by the pimpleDymFoam algorithm, an unsteady turbulent solver in the OpenFOAM package. The time-step size was set such that the maximum Courant number was less than 1 throughout the domain.

The freestream velocity was set to 3.77 m/s, resulting in a Reynolds number of 30,000 based on chord length. Constant velocity at the inlet, zero gradient velocity with a constant pressure at the outlet, no slip condition along the surfaces of the airfoils, and spatially periodic condition in the spanwise direction were applied to the boundary conditions. Periodic boundary condition is typically assumed in large-eddy simulations over domains with a homogeneous direction. This situation corresponds to a wing of infinite aspect ratio. To allow for pitching motion, a circular sliding interface around the forefoil was implemented to separate moving and stationary zones. The boundary conditions are presented in Fig. 2.

Fig. 2. Computational domain and applied boundary conditions.

2.3 Computational domain and grid

The computational domain extended approximately 14 chord lengths upstream of the forefoil and 18 chord lengths downstream of the hindfoil. A three-dimensional domain was generated by extruding the 2-D domain by a length of s=0.1C in the spanwise direction, as shown in Fig. 2 (for better clarity, the dimensions along the Z-axis are shown on an enlarge scale). Carta et al. [24] also used a span size of s=0.1C for a single pitching airfoil study. Visbal [25] also examined the spanwise extent on a single plunging airfoil for s=0.1C to s=0.8C and stated that the smallest span size predicted the main structures quite well.

A structured grid was generated for the entire domain. Grid points were concentrated near the airfoils, especially around the leading-edges to capture the onset of dynamic-stall and vortex-interaction. A circular structured grid around the forefoil was implemented. The grid inside this circular zone moved with the airfoil like a rigid-body motion without grid deformation. The generated grid around the forefoil and hindfoil is presented in Fig. 3.

According to Piomelli and Chasnow [26], the requirement to capture a fully resolved wall for LES simulations is $Y^+ < 2$, $X^+ = O(50\text{-}150)$, and $Z^+ = O(15\text{-}40)$, where Y^+ is the first cell layer thickness in wall units and X^+ and Z^+ are the wall-grid spacings in the streamwise and spanwise directions in wall units, respectively. The distribution of Y^+, X^+, and Z^+ on the upper surface of the forefoil at a nondimensional time of t/T=0.4, and on the upper surface of the hindfoil at a nondimensional time of t/T=0.8 for three sections in Z direction are presented in Fig. 4 and Fig. 5, respectively. As will be presented in an upcoming

section, the nondimensional times of t/T=0.4 and t/T=0.8 correspond to the moments of convection of a leading-edge vortex (LEV) on the upper surface of the forefoil and the collision of the LEV with the leading-edge of the hindfoil, respectively. The height of the first cell (adjacent to the surfaces of the airfoils) was set to ensure a Y^+ value lower than 1. The X^+ and Z^+ values were also well within the ranges for both airfoils. The final grid used in this study contained approximately 18 million cells.

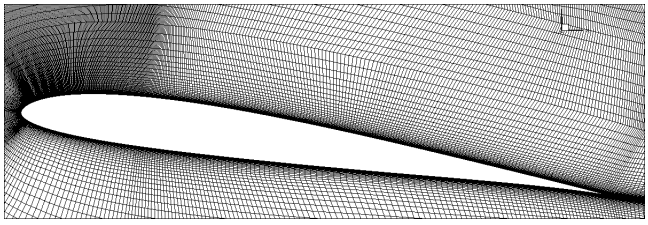

(a)

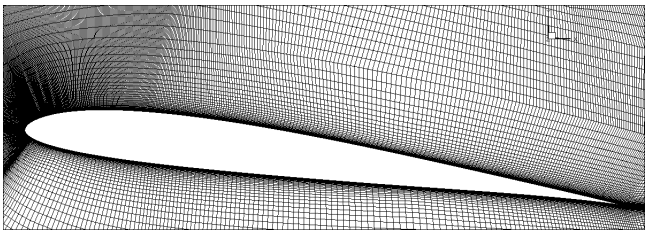

(b)

Fig. 3. Grid of (a) the forefoil and (b) the hindfoil**.**

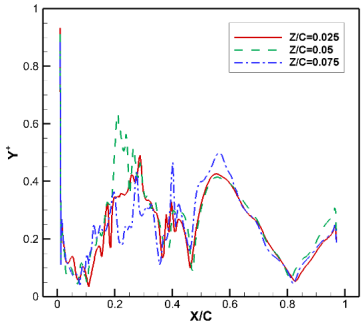

(a)

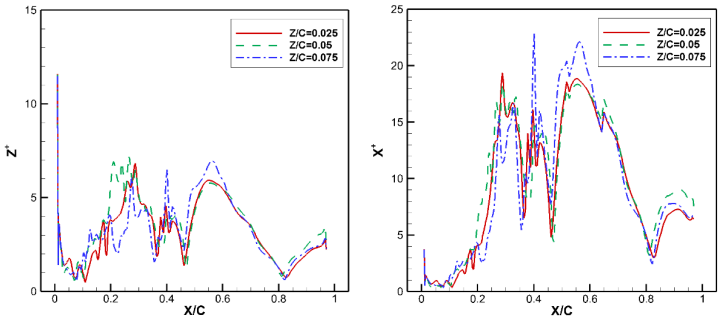

(b) (c)

Fig. 4. Distribution of (a) Y^+, (b) Z^+, and (c) X^+ on the upper surface of the forefoil at t/T=0.4.

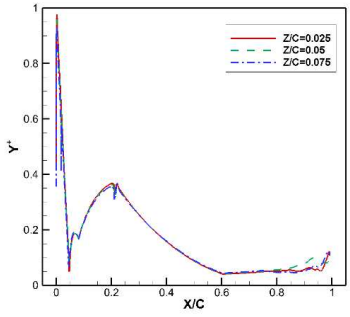

(a)

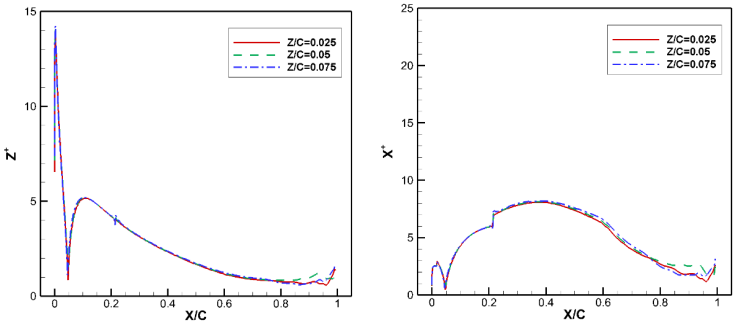

(b) (c)

Fig. 5. Distribution of (a) Y^+, (b) Z^+, and (c) X^+ on the upper surface of the hindfoil at t/T=0.8.

3. VALIDATION

To validate the numerical approach, the results from LES simulation of flow over a single pitching SD7003 airfoil at Reynolds number of Re=30,000 and reduced frequency of K=0.25 were compared with the available data: LES study of Carta et al. [24] for a single pitching SD7003 airfoil, LES study of Visbal [25] and PIV experimental studies of Baik et al. [27] for a single SD7003 airfoil with an equivalent pure-plunge motion. Data from the study of Baik et al. included two different water-channel facilities located at the US Air Force Research Laboratory (AFRL) and the University of Michigan (UM). All the mentioned studies were performed at a Reynolds number of Re=60,000 and reduced frequency of K=0.25. The comparison of the phase-averaged spanwise vorticity and streamwise velocity contours at four phases of the oscillation cycle are presented in Fig. 6 and Fig. 7, respectively. At phases Φ=90° all studies indicated the formation of a large clockwise leading-edge vortex (LEV). The size of the LEV in UM is smaller compared to other studies. At the same time, a counterclockwise vortex was also formed underneath the leading-edge vortex, which is more evident in the numerical results. At Φ=120°, this vortex was about to cut the LEV feeding sheet, which is more pronounced in the computations. The LEV continued to move along the airfoil until it was shed at Φ=150. The separation region developed as the LEV moved along the upper surface of the airfoil until Φ=150 for all studies. By Φ=150, the entire upper surface of the airfoil was separated, as shown in Fig. 7. The approach of the LEV towards the trailing-edge led to the formation of a trailing-edge vortex (TEV). This vortex in all studies was larger than the experimental results, especially the AFRL results. At Φ=210˚, a shear layer separated from the leading-edge was visible for all studies. In this phase, the flow was about to attach to the surface. The velocity contour of the current study was more similar to LES by Visbal compared to the experimental data. Overall, all simulations and experiments exhibited similar characteristics. According to Fig. 6 and Fig. 7, the formation of LEV and TEV was well predicted in current study, so there was a good agreement between the results of the present study and the other studies.

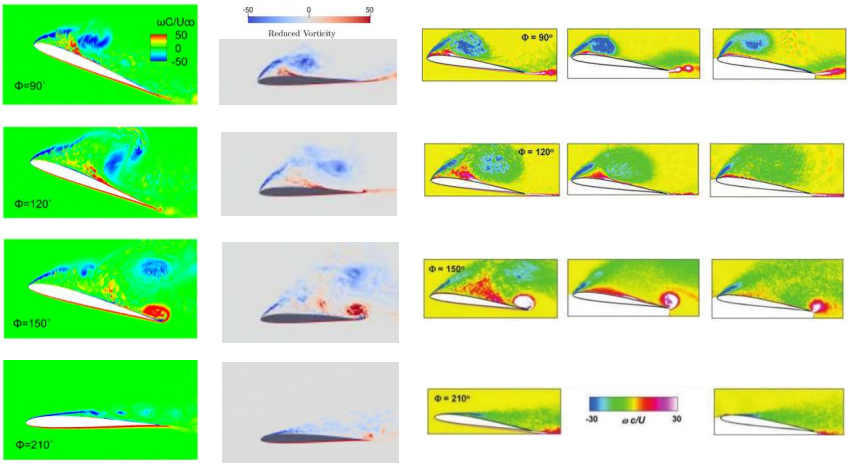

(a) (b) (c) (d) (e)

Fig. 6. Comparison of the phase-averaged spanwise vorticity of (a) current study with numerical studies of (b) [24] (LES) and (c) [25] (LES), and experimental studies of (d) [27] (PIV, UM) and (e) [27] (PIV, AFRL) at different

phases. (b) was reproduced from M. Carta, R. Putzu, T. Ghisu. A comparison of plunging- and pitching-induced deep dynamic stall on an SD7003 airfoil using URANS and LES simulations. Aerosp. Sci. Technol. 2022; 121: 107307. Copyright © 2021, Elsevier Masson SAS. All rights reserved. (c-e) were reproduced from M. R. Visbal. Numerical investigation of deep dynamic stall of a plunging airfoil. AIAA J. 2011; 49: 2152-2170. Public Domain

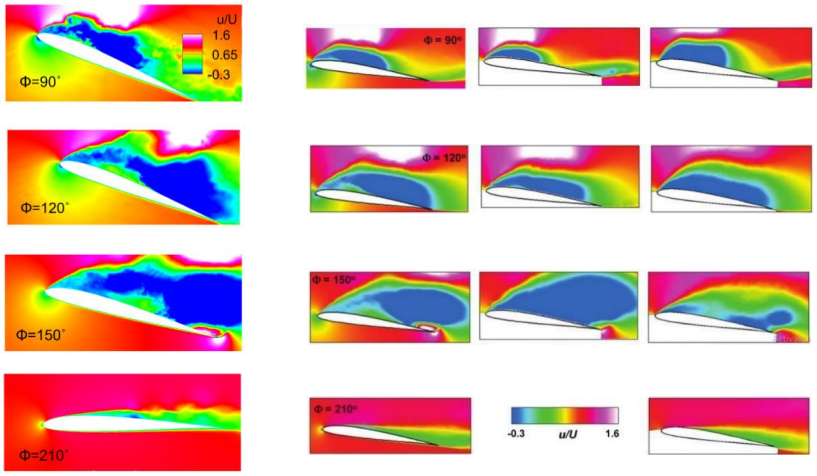

(a) (b) (c) (d)

Fig. 7. Comparison of the phase-averaged streamwise velocity of (a) current study with the numerical studies of (b) [25] (LES), and the experimental studies of (c) [27] (PIV, UM) and (d) [27] (PIV, AFRL) at different phases. (b-d) were reproduced from M. R. Visbal. Numerical investigation of deep dynamic stall of a plunging airfoil. AIAA J. 2011; 49: 2152-2170. Public Domain.

In Fig. 8, the pressure coefficient and skin friction coefficient over the upper surface of the airfoil are compared with the study of Carta et al. at three phases of pitching motion. Variations of pressure coefficient and skin friction coefficient due to the presence of the leading-edge vortex and the trailing-edge vortex were well predicted. The maximum and minimum values were slightly different.

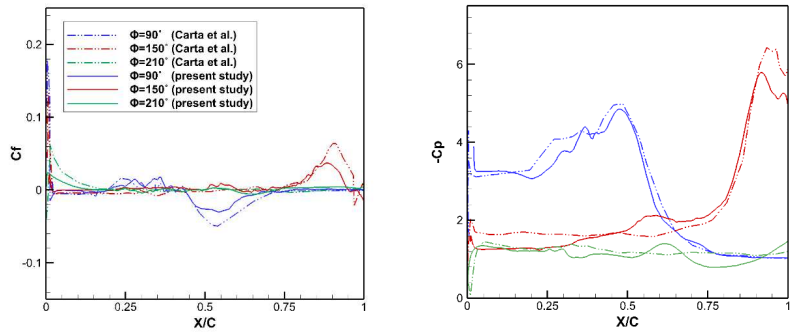

(a) (b)

Fig. 8. Comparison of (a) skin friction coefficient and (b) pressure coefficient on the upper surface of the airfoil with numerical results of [24] at three phases.

In another comparison, the lift coefficient of the oscillating airfoil during an oscillating cycle was compared with LES results. This comparison is presented in Fig. 9. According to Fig. 9, the current results showed good agreement for the upstroke motion and the peak value, especially with the study of Carta et al. for pitching motion. For the downstroke motion, the current simulation underpredicted the lift coefficient compared to the other studies. However, there was the most agreement with the study of Visbal during this phase.

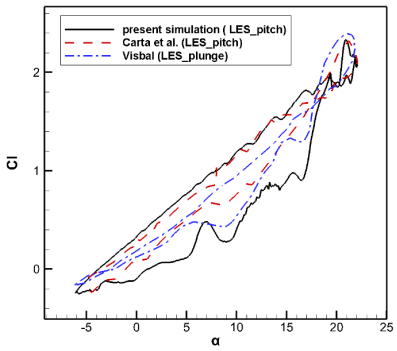

Fig. 9. Comparing the lift coefficient with [24] and [25] references during an oscillating cycle.

4. RESULTS AND DISCUSSION

4.1. Comparison with URANS

In this section, the results from a 2-D URANS simulation were compared with the results from a 3-D LES simulation, including the flowfield and the aerodynamic coefficients. The angle of attack of the

hindfoil and the location of it in a tandem configuration for the 2-D URANS simulation was obtained through an optimization study in our previous work to maximize the total lift-to-drag ratio of the airfoils in tandem configuration. The reader may refer to reference [21] for more details. Both simulations were performed at a Reynolds number of Re=30,000. The forefoil oscillated with a pure-pitch motion at a reduced frequency of K=0.5, mean angle of attack of α_0=8°, and amplitude of A=14.1°. This high pitching amplitude put the forefoil into a deep dynamic stall. The horizontal and vertical spacing between the airfoils were fixed at l=2.62C and h=0.44C, respectively. The angle of attack of the hindfoil was set to α=7.216°. The phase-averaged spanwise vorticity contour of LES is presented in Fig. 10 and is compared with the results from URANS during one pitching cycle. Phase-averaged lift and drag coefficients are presented in Fig.11 for both simulations. According to Fig. 10, several vortices were produced in 3-D LES similar to 2-D URANS during the cycle. The formation of a clockwise (CW) vortex followed by a main leading-edge vortex on the forefoil is evident at the beginning of the cycle (Fig. 10(b)). Next, the formed CW vortices moved on the forefoil and led to the formation of counterclockwise (CCW) vortices at the trailing-edge by approaching the trailing-edge (Fig. 10(d)). The strength of the CCW vortices created on the trailing-edge was affected by the strength of the corresponding CW vortices. The main LEV led to the formation of a relatively large TEV. Finally, the vortices (CW and CCW) shed from the forefoil at different moments. At the end of the cycle, by increasing the angle of attack of the forefoil, the flow was attached to the surface again.

The approach of the LEV and TEV had a significant effect on the aerodynamics of the hindfoil. As the LEV approached the hindfoil, the streamlines bent such that the effective angle of attack of the hindfoil reduced and led to a reduction in lift and drag coefficients of the hindfoil for both simulations, as shown in Fig. 11(c) and (d). The LEV also induced the formation of a small CCW vortex on the lower surface of the hindfoil. Once the LEV hit the hindfoil, it split into two pieces, and the lift and drag increased rapidly. At this point, the angle of attack of the hindoil was minimum, and after this stage, the angle of attack began to increase immediately. After the interaction of the LEV and TEV with the hindfoil, the hindfoil was still influenced by small shedding vortices from the forefoil. These vortices were created due to the upper surface separation of the forefoil. In a single configuration of the hindfoil, only a laminar separation bubble would be created on the upper surface of the airfoil, whereas in the tandem configuration, multiple vortices would be created after the first and second interactions, completely altering the aerodynamic behavior of the hindfoil. To be more specific, the hindfoil was influenced by the flowfiled of the forefoil for the entire pitching cycle. The formation of vortices on the forefoil, especially the LEV, altered the flow around the hindfoil. From the beginning of the formation of the LEV, the streamlines near the hindfoil began to change, and the rate of this change increased as the LEV approached the hindfoil. The presence of the hindfoil had a minor effect on the forefoil.

By comparing the contours of LES and URANS (Fig. 10), it is apparent that URANS underpredicted the strength of the vortices compared to LES. This lower strength is more evident in LEV and TEV. According to the pressure coefficient distribution on the upper surface of the forefoil presented in Fig. 12(a), and (b), the locations of the two CW vortices on the forefoil surface and the amount of pressure reduction due to their presence were similar to URANS at t/T=0.25. However, the third CW vortex formed in URANS was not observed in LES at t/T=0.5 (Fig. 10(c) and (i)). This difference is also clear in the pressure coefficient of Fig. 12(b). The LEV also led to a higher-pressure reduction and a different location at this time (t/T=0.5) for LES compared to the URANS, which indicated a delay in the movement of the LEV compared to the URANS. The delay in LEV and TEV shedding from the forefoil is more evident in Fig. 10(d) and Fig. 10(j). The LEV fed off the leading-edge vorticity. The formation of a region with negative vorticity upstream of the LEV cut the LEV feeding and caused the loss of LEV strength and faster convection. For LES, this area with negative vorticity was much smaller than URANS and led to a delay in

shedding the LEV from the forefoil. Cutting LEV feeding caused the formation of the third CW vortex in URANS.

The delay in LEV shedding also resulted in a delay in interaction with the hindfoil. This delay is evident in Fig. 11(c) and (d). Due to the increased strength of the vortices in LES, the streamlines around the hindfoil were more bent, causing further reduction in the lift and drag of the hindfoil as the LEV approached the hindfoil. The reduction in drag was significant enough to generate thrust on the hindfoil for both approaches, especially in LES. The cores of the LEV and TEV dissipated completely in URANS, whereas they persisted downstream of the hindfoil with a relatively high vorticity magnitude in LES as shown in Fig 10 (a) and (g). According to the pressure coefficient of the hindfoil (Fig. 12(c) and (d)), there were more severe fluctuations in the front part of the airfoil at t/T=0 for URANS. It was due to the formation of multiple vortices. There was a higher pressure drop due to the LEV collision at t/T=0.75 for URANS. In the other two moments, the pressure variations were very close for the two approaches.

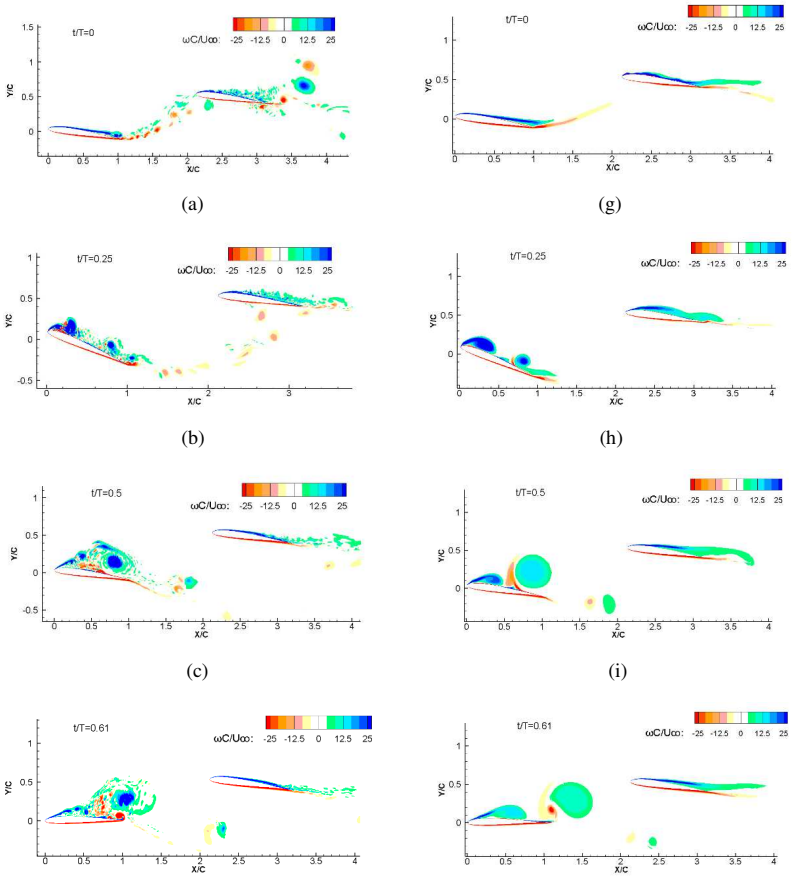

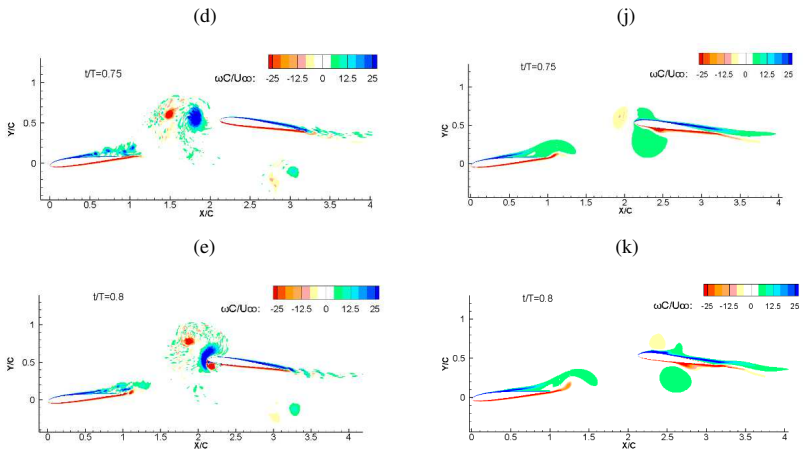

Fig. 10. Phase-averaged vorticity contour comparison between (a)-(f) LES and (g)-(l) URANS for a pitching cycle.

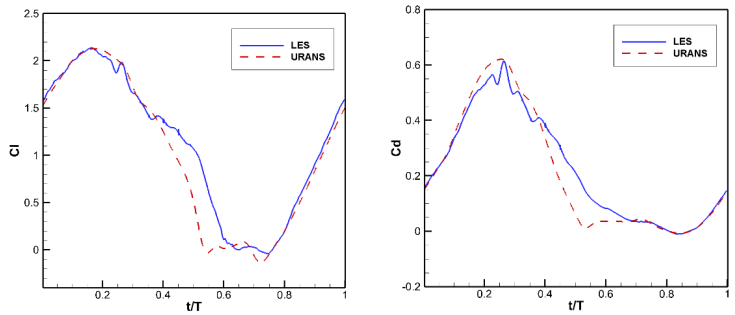

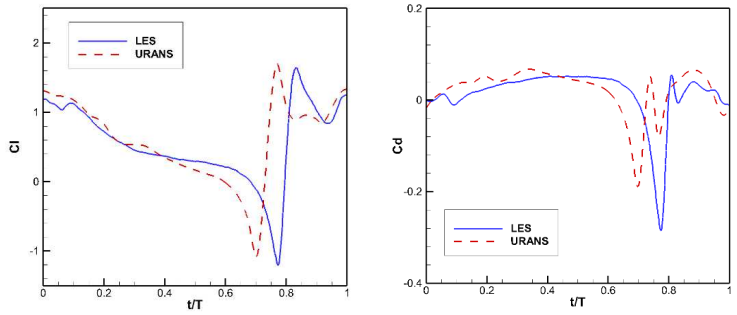

(c) (d)

Fig. 11. Phase-averaged lift and drag coefficients of (a), (b) the forefoil and (c), (d) the hindfoil for URANS and LES.

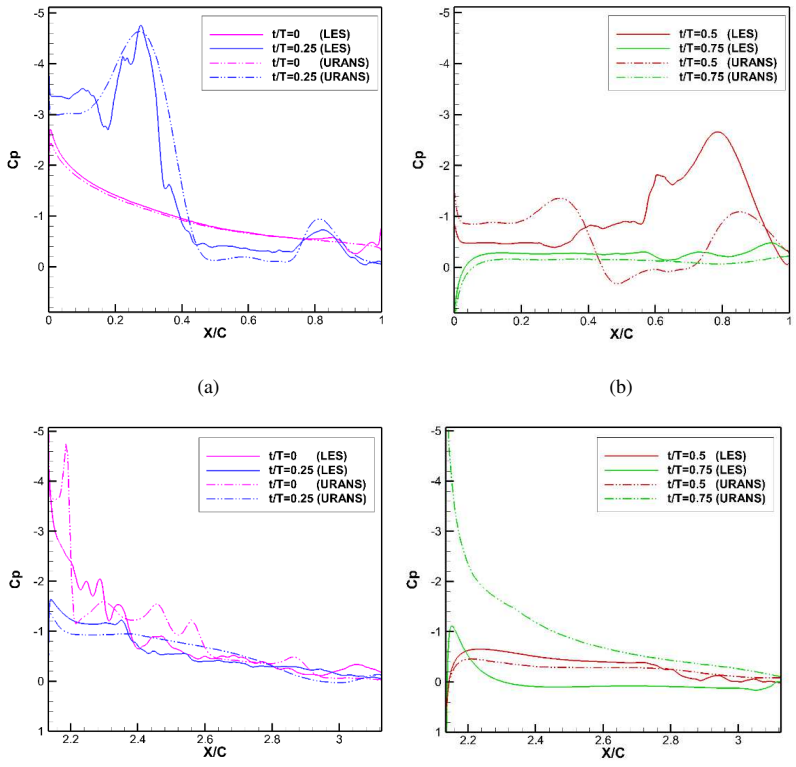

(a) (b)

(c) (d)

Fig. 12. Phase-averaged pressure coefficient on the upper surface of (a), (b) the forefoil, and (c),(d) the hindfoil for URANS and LES at several moments.

The LEV trajectory for both approaches is determined by monitoring the point of maximum vorticity of LEV core over time, as shown in Fig. 13. It starts from the initial moments of LEV formation on the forefoil to the moments of interaction with the hindfoil. After the interaction, the core of LEV was tracked. The delay in LEV convection and shedding for LES compared to URANS is evident in Fig. 13. This delay changed the LEV interaction with the hindfoil such that the core of the LEV took different paths for each approach.

In Table 1, the time-averaged aerodynamic coefficients for LES and URANS are presented and compared. The tandem configuration and vortex interaction significantly lowered the drag coefficient of the hindfoil, resulting in a negative time-averaged drag coefficient (thrust) in LES. The time-averaged values of lift and drag coefficients predicted by URANS were higher than those predicted by LES, which resulted in a 23% aerodynamic performance (lift-to-drag ratio) error for the URANS simulation.

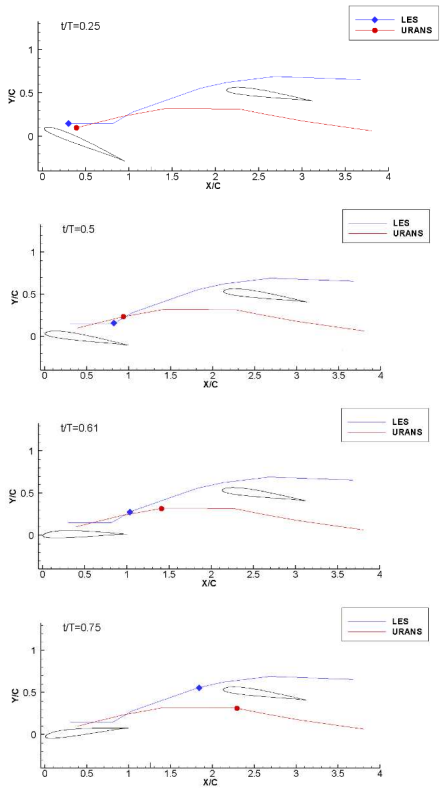

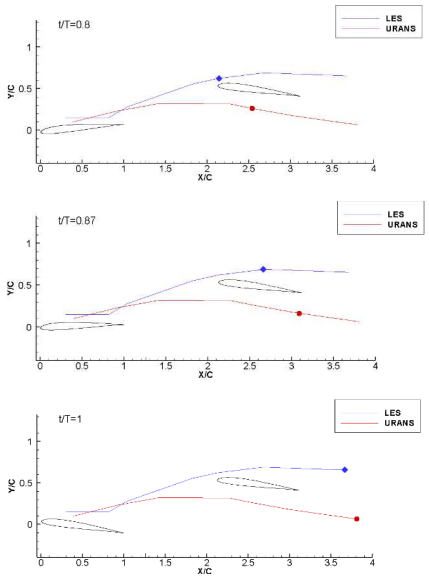

Fig. 13. Comparison between URANS and LES for LEV trajectory.

Table 1. Comparison between URANS and LES for time-averaged aerodynamic coefficients.

Case	Cl_f	Cl_h	Cd_f	Cd_h	Cl_f+Cl_h	Cd_f+Cd_h	L/D_{tot}
LES	1.079	0.625	0.197	-0.005	1.704	0.193	8.85
URANS	1.006	0.585	0.212	0.021	1.592	0.233	6.84

4.2. Turbulence characteristics

Turbulence characteristics of the tandem configuration's flowfield were investigated using large-eddy simulation. Turbulence characteristics, including turbulent kinetic energy, Reynolds stress, and isosurfaces of the Q-criterion, are presented at several phases in the pitching cycle.

Large-eddy simulations are required to resolve large turbulent structures by the generated grid, while the structures smaller than the size of the grid cells are modeled (sgs). The contour of the phase-averaged resolved turbulent kinetic energy (k_{res}) and modeled turbulent kinetic energy (k_{sgs}) at different phases are presented in Fig. 14, columns (a) and (b), respectively. The resolved turbulent kinetic energy was calculated from the velocity fluctuations according to the relation $k_{res.} = (\langle u'u' \rangle + \langle v'v' \rangle) + \langle w'w' \rangle)/2$, whereas the modeled component was obtained as $k_{sgs} = (\nu_{sgs}/C_s\Delta)^2$. According to Fig. 14, a significant portion of the turbulent kinetic energy was carried by the vortices, especially the LEV and TEV. At the beginning of the cycle, the turbulent kinetic energy around the forefoil only existed near the trailing-edge. As the angle of attack of the forefoil increased and vortices were generated, the turbulent kinetic energy levels also rose.

Upon shedding the vortices from the forefoil, the energy began to convect downstream and was transferred to the hindfoil, which initially contained a very small amount of energy prior to interaction. After the interaction, the flow over the hindfoil became completely turbulent.

The size of the grid cells needs to be determined in such a way that a high percentage of the turbulent kinetic energy is resolved and the rest is modeled. To make sure that the LES results are reliable, about 80% of the total turbulent kinetic energy should be resolved [28]. The total turbulent kinetic energy is calculated as the sum of resolved turbulent kinetic energy and modeled turbulent kinetic energy. Fig. 15 shows the contour of the ratio of resolved turbulent kinetic energy to total turbulent kinetic energy at various phases around both airfoils. The generated grid resolved more than 80% of the total turbulent kinetic energy, showing the desirability of the generated grid.

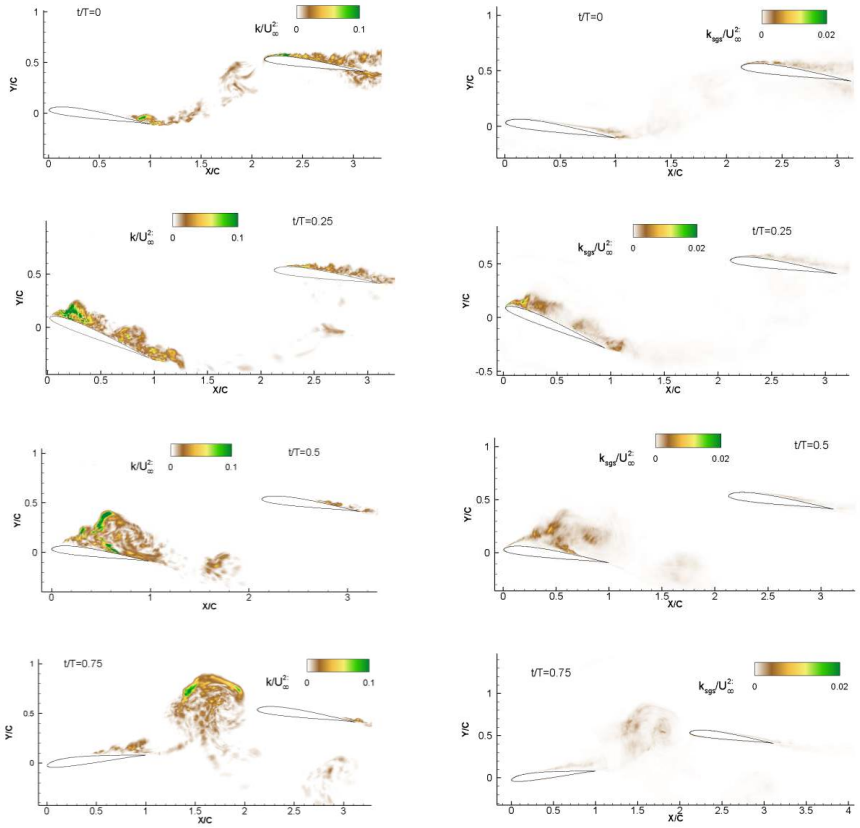

Fig. 14. (a) Resolved and (b) modeled turbulent kinetic energy.

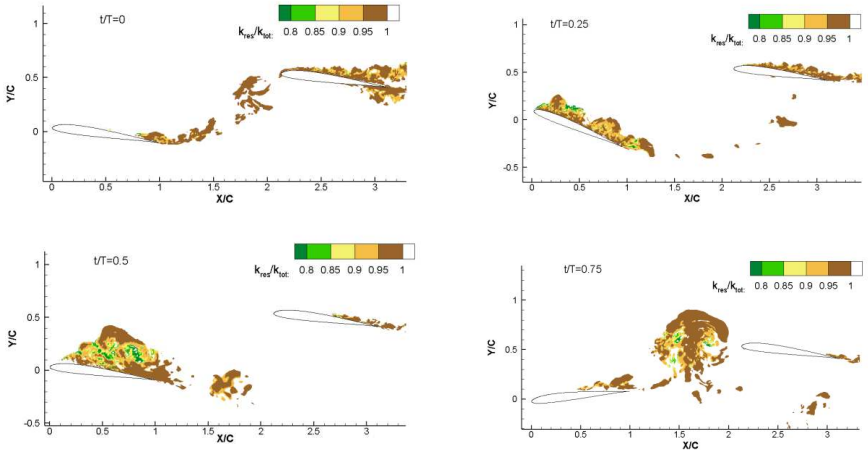

Fig. 15. Ratio of resolved turbulent kinetic energy to total turbulent kinetic energy.

The phase-averaged resolved Reynolds stress (u'v') and modeled SGS stress (τ^*_{12}) are shown in Fig. 16. The values of both stresses increased with the formation of the vortices and flow separation on the forefoil. The maximum stress was observed within the LEV and the TEV, which was transferred by the convection of these vortices. The stress inside the LEV was mostly negative. The changes were very similar to the turbulent kinetic energy. The regions with the highest values of turbulent kinetic energy (green areas in Fig. 14(a)) mostly exhibited negative stress (blue areas in Fig. 16(a)).

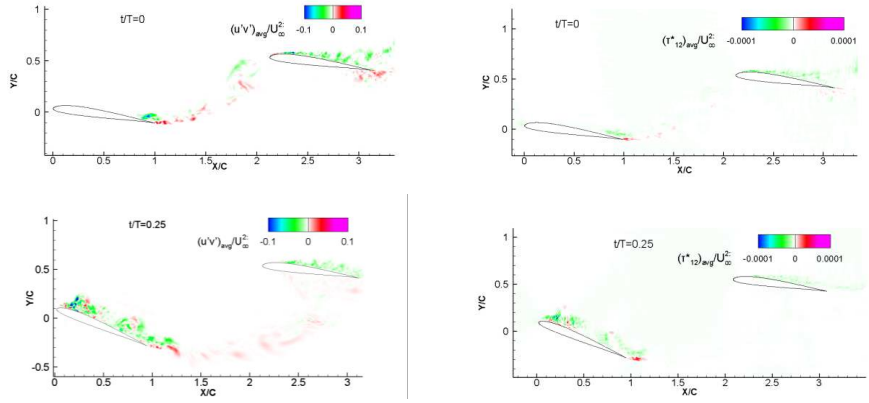

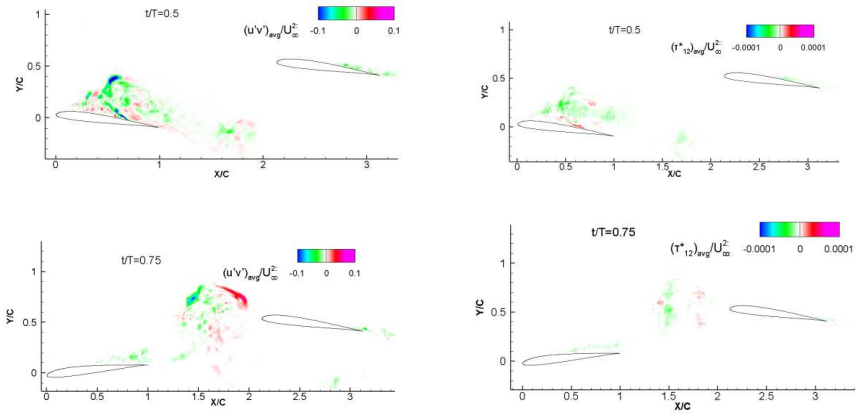

(a) (b)

Fig. 16. Phase-averaged (a) resolved Reynolds stress and (b) modeled SGS stress.

In the study of the Reynolds stress of the flow field, the variation of the normal stress value (u'u') was also investigated by examining the profile of (u'_{rms}). The distribution of (u'_{rms}) at different locations on the forefoil and hindfoil equal to X/C=0.12, 0.25, 0.50, 0.75, and 1 are presented in Fig. 17 at several moments of an oscillation cycle. According to the values of normal stress on the forefoil (Fig. 17(a)), the main normal stress variations were related to the LEV. The maximum normal stress on the forefoil was occurred at X/C=0.25 at t/T=0.25, corresponding to the formation of the LEV during the initial stages. After the formation and movement of the LEV on the airfoil, the stress spread in a wider range (t/T=0.5), but the peak value decreased. At t/T=0 and t/T=0.75, the normal stress on the forefoil was very small, especially for the front part of the forefoil. The maximum stress on the hindfoil occurred at t/T=0 at X/C=0.12, in a very small vertical spacing after the collision of the vortices with the hindfoil. The normal stress on each location decreased over time until it reached the lowest values (Fig. 17(b)).

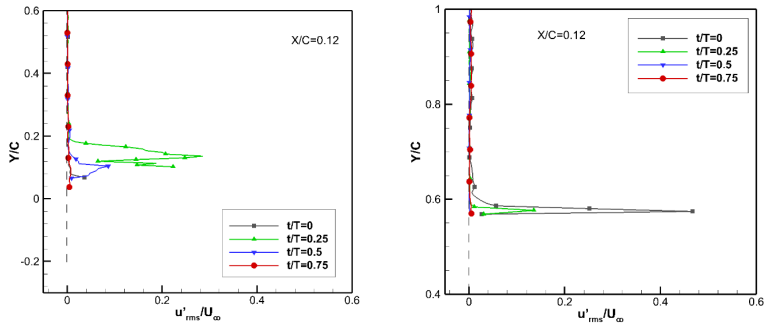

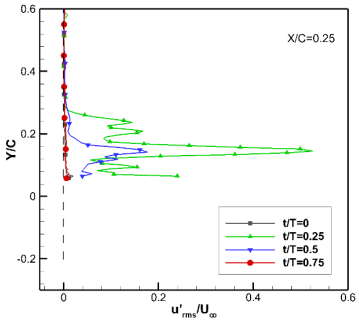
X/C=0.25
Y/C
u'rms/U∞
t/T=0
t/T=0.25
t/T=0.5
t/T=0.75

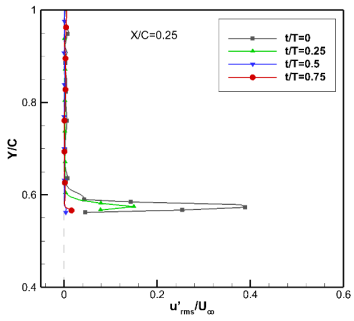
X/C=0.25
Y/C
u'rms/U∞
t/T=0
t/T=0.25
t/T=0.5
t/T=0.75

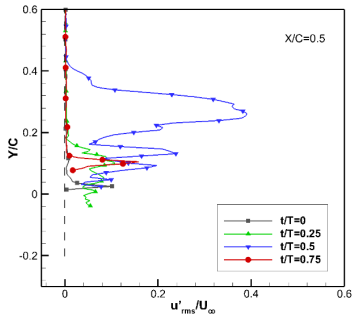
X/C=0.5
Y/C
u'rms/U∞
t/T=0
t/T=0.25
t/T=0.5
t/T=0.75

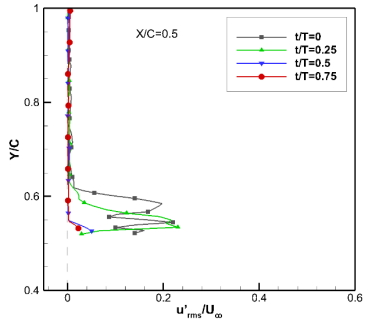
X/C=0.5
Y/C
u'rms/U∞
t/T=0
t/T=0.25
t/T=0.5
t/T=0.75

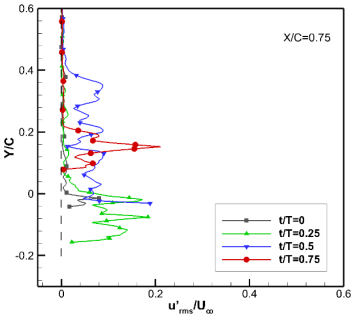
X/C=0.75
Y/C
u'rms/U∞
t/T=0
t/T=0.25
t/T=0.5
t/T=0.75

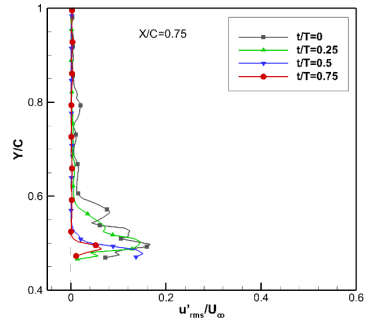
X/C=0.75
Y/C
u'rms/U∞
t/T=0
t/T=0.25
t/T=0.5
t/T=0.75

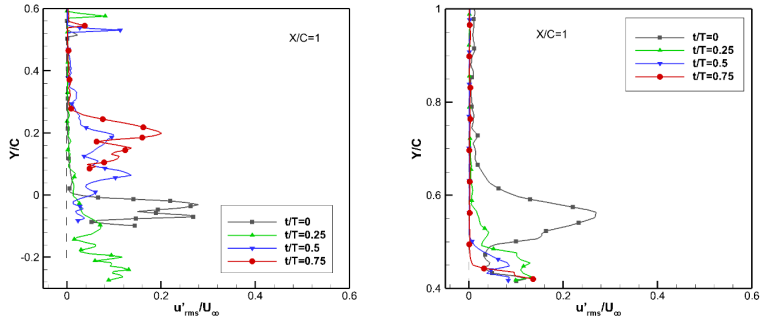

Fig. 17. Comparison of u'_{rms} profile at different locations (X/C) on the (a) forefoil and (b) the hindfoil at different moments.

Fig. 18 presents the Q-criterion isosurfaces colored by streamwise velocity. The Q-criterion is a scalar field to identify vortices in a flowfield. It is defined as the second invariant of the velocity gradient tensor [29] and is calculated as $Q=\frac{1}{2}(\|\Omega\|^2-\|S\|^2)$, where $\|\Omega\|^2=\mathrm{trace}(\Omega\Omega^T)$, $\|S\|^2=\mathrm{trace}(SS^T)$, and Ω and S are the rotation tensor and strain rate tensor, respectively. A positive Q value indicates that the local flow has more rotational motion than strain. As shown in Fig. 18 (b), (c), the leading-edge instability that leads to the transition from laminar to turbulent flow and the formation of K-H (Kelvin-Helmholtz) instabilities are evident. These instabilities led to the production of two-dimensional rolls. These rolls were finally broken and created three-dimensional structures. At t/T=0.25, when the LEV was near the leading-edge, the entire surface of the forefoil became turbulent. Over time, the LEV increased in size and moved downstream. Structures related to the vortices were larger in size compared to the other structures and contained the highest amount of turbulent kinetic energy of the flowfield. These structures were mainly needle-shaped, and kept their needle-shaped while moving downstream. These structures are evident in Fig. 18 in the upstream part of CW vortices. In addition to the needle-shaped structures, the hairpin structures were also formed on the airfoils. The dominant structures on the forefoil were related to the LEV until it shed from the forefoil. After the shedding of LEV, only smaller structures remained on the forefoil. As the angle of attack of the forefoil increased, the boundary layer reattached to the surface, and the flow over the leading-edge became laminar, so there was no structure in the front half of the airfoil.

After the collision of the vortices carrying significant turbulent kinetic energy with the hindfoil, the large and needle-shaped structures were broken into smaller ones, and the entire upper surface of the hindfoil was disturbed. The rear of the lower surface of the hinfoil also experienced turbulence with small structures (Fig 18(a)). A tube-shaped structure was also formed near the trailing-edge of the hindfoil. These disturbances decreased on the hindfoil over time by elimination of the source of turbulence, leading to the laminarization of the flow in most parts of the surface. At t/T=0.75, hairpin structures were apparent near the trailing-edge of the hindfoil, while the flow transitioning to laminar from the leading-edge of the hindfoil.

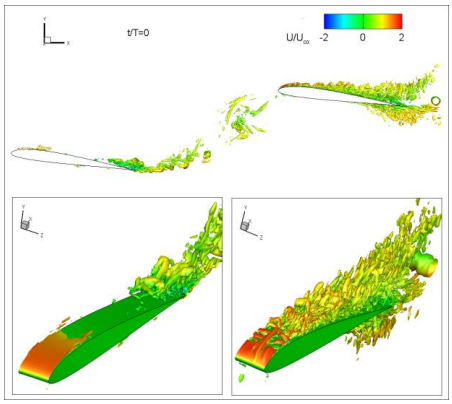

(a)

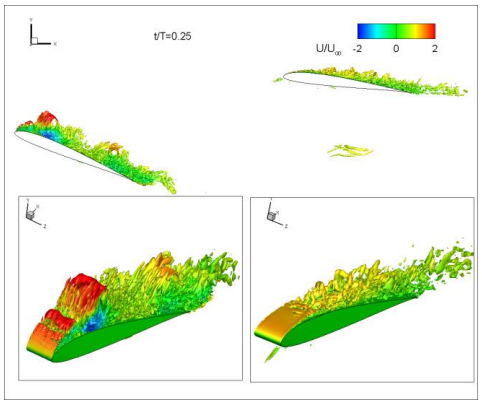

(b)

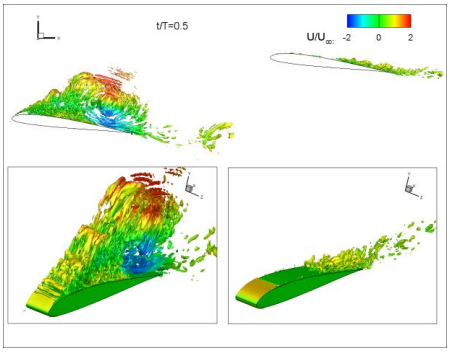

(c)

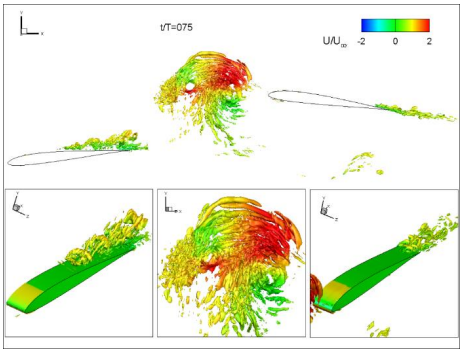

(d)

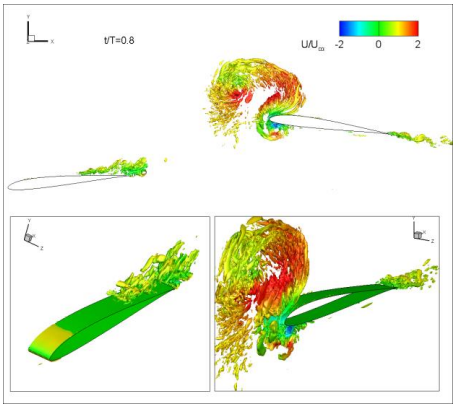

(e)

Fig. 18. Instantaneous three-dimensional flow structures at selected moments of the pitching cycle displayed in terms of Q-criterion isosurface (Q=100,000).

5. CONCLUSIONS

Large-eddy simulation approach was applied to two airfoils in tandem configuration with a pitching SD7003 forefoil and a stationary SD7003 hindfoil at a Reynolds number of Re=30,000. Dynamic stall over the forefoil caused by rapid pitching motion and the vortex interaction between the hindfoil and the vortices created by the forefoil were investigated. The forefoil oscillated with a reduced frequency of K=0.5 and an amplitude of 14.1˚ for a mean angle of attack of 8˚.

The unsteady flow structures were described with emphasis on the formation of a leading-edge vortex (LEV) on the forefoil. Turbulence characteristics of the tandem configuration such as turbulent kinetic energy and Reynolds stress of the flowfield during different phases of a pitching cycle were investigated. They were mainly created by the formation of vortices, especially the leading-edge vortex on the forefoil, and they were transferred downstream to the hindfoil by vortex shedding, making the flow over the hindfoil completely turbulent. Maximum stress was observed within the LEV and TEV. The normal stress variations on the forefoil were primarily related to the LEV, with peak values occurring at specific points in the pitching cycle. The normal stress had the maximum value at the beginning of the pitching cycle with the formation of the LEV. Also, the maximum normal stress on the hindfoil was observed near the leading-edge, which was created after the interaction with the shed vortices, diminishing over time. Its value was on the order of the normal stress produced by the LEV on the forefoil,

Transitional aspects of the flow were investigated by examining the isosurfaces of the Q-criterion. Kelvin–Helmholtz type instabilities were generated in the boundary layer of the upper surface of the forefoil at the start of the upstroke phase, revealing the transition from laminar to turbulent flow. Then, a LEV composed of multiple vortical structures was formed. The structures related to the LEV were mostly needle-shaped and maintained their needle shape with the movement of the vortex. These structures broke into multiple smaller structures after interaction with the hindfoil.

This study also presented a description of the differences between two-dimensional URANS and three-dimensional LES for the prediction of the above flow case. The two-dimensional URANS approach was capable of predicting the main vortices but was unable to predict the correct evolution of the region with negative vorticity, which was formed upstream of the LEV. This region cut off the connection between LEV and the leading-edge. As a result, LEV convected faster, which led to an earlier collision with the hindfoil compared to the LES approach. URANS predicted higher lift and drag coefficients than LES, resulting in a 23% error in the lift-to-drag ratio. Nevertheless, the results indicated the appropriate approximation of URANS. URANS approach was capable of capturing major flow physics such as the general formation and movement of vortices, the overall aerodynamic coefficients, and basic interaction patterns. It predicted the formation of large structures well but was not accurate enough in predicting the evolution of small structures compared to LES. LES provided a more detailed and accurate representation of vortex strength and interactions, showing a clear delay in LEV convection and shedding compared to URANS.

ACKNOWLEDGMENTS

We acknowledge the CINECA award under the ISCRA initiative, for the availability of high-performance computing resources and support.

DATA AVAILIBILITY

The data that support the findings of this study are available from the corresponding author upon reasonable request.

REFERENCES

[1] I. Fenercioglu, O. Centiner," Categorization of flow structures around a pitching and plunging airfoil," J. Fluids Struct. 31, 92-102 (2012).

[2] H. Liang, K. Ou, S. Premasuthan, A. Jameson, and Z. J. Wang, "High-order accurate simulations of unsteady flow past plunging and pitching airfoils," Computers and Fluids 40, 236-248 (2010).

[3] M. Thakor, G. Kumar, D. Das, and A. De, "Investigation of asymmetrically pitching airfoil at high reduced frequency," Phys. Fluids 32, 053607 (2020).

[4] K. Lu, Y. H. Xie, and D. Zhang, "Numerical study of large amplitude, nonsinusoidal motion and camber effects on pitching airfoil propulsion," J. Fluids Struct. 36, 184-194 (2013).

[5] J. Han, Z. Yuan, and G. Chen, "Effects of kinematic parameters on three-dimensional flapping wing at low Reynolds number," Phys. Fluids 30, (2018).

[6] S. Sarkar, "Comparing pure-pitch and pure-plunge kinematics for a symmetric airfoil," AIAA J. 48, (2010).

[7] M. R. Visbal, "High-fidelity simulation of transitional flows past a plunging airfoil," AIAA J. 47, (2009).

[8] N. Guillaud, G. Balarac, and E. Goncalves, "Large eddy simulations on a pitching airfoil: Analysis of the reduced frequency influence," Computers and Fluids 161, 1-13 (2018).

[9] M. A. Ashraf, J. Young, and J. C. S. Lai, "Oscillation frequency and amplitude effects on plunging airfoil propulsion and flow periodicity," AIAA J. 50, (2012).

[10] J. M. Yu, T. S. Leu, and J. J. Miau, "Investigation of reduced frequency and freestream turbulence effects on dynamic stall of a pitching airfoil," J. Vis. 20, 31-44 (2017).

[11] C. Zhu, J. Chen, J. Wu, and T. Wang, "Dynamic stall control of the wind turbine airfoil via single-row and double-row passive vortex generators," Energy 189, (2019).

[12] L. Guoqiang, Y. Shihe, "Large eddy simulation of dynamic stall flow control for wind turbine airfoil using plasma actuator," Energy 212, (2020).

[13] N. Hosseini, M. Tadjfar, and A. Abba, “Flow control with synthetic jets on two tandem airfoils using machine learning,” Phys. Fluids 35, 027114 (2023).

[14] W. B. Tay, H. Bijl, and B. W. van Oudheusden, “Biplane and tail effects on flapping flight,” AIAA J. 51, (2013).

[15] J. Wu, G. Li, L. Chen, and Y. Zhang, “Unsteady aerodynamic performance of a tandem flapping–fixed airfoil configuration at low Reynolds number,” Phys. Fluids 34, 111907 (2022).

[16] X. Meng, Z. Chen, Y. Zhang, G. Chen, “Aerodynamic performance and flow mechanism of multi-flapping wings with different spatial arrangements,” Phys. Fluids 34, 021907 (2022).

[17] R. Jurado, G. Arranz, O. Flores, and M. Garcia-Villalba, “Numerical simulation of flow over flapping wings in tandem: wingspan effects,” Phys. Fluids 34, 017114 (2022).

[18] G. D. Xu, W. Y. Duan, and W. H. Xu, “The propulsion of two flapping foils with tandem configuration and vortex interactions,” Phys. Fluids 29, 097102 (2017).

[19] T. M. Broering, Y. Lian, “Numerical investigation of energy extraction in a tandem flapping wing configuration,” AIAA J. 50, (2012).

[20] Z. Chen, X. Li, and L. Chen, “Enhanced performance of tandem plunging airfoils with an asymmetric pitching motion,” Phys. Fluids 34, 011910 (2022).

[21] N. Hosseini, M. Tadjfar, and A. Abba, “Configuration optimization of two tandem airfoils at low Reynolds numbers,” Appl. Math. Model. 102, 828-846 (2022).

[22] T. Ji, F. Jin, F. Xie, et al., “Active learning of tandem flapping wings at optimizing propulsion performance,” Phys. Fluids 34, 047117 (2022).

[23] D. K. Lilly, “A proposed modification of the Germano subgrid-scale closure method,” Phys. Fluids 4, 633-635, (1992).

[24] M. Carta, R. Putzu, and T. Ghisu, “A comparison of plunging- and pitching-induced deep dynamic stall on an SD7003 airfoil using URANS and LES simulations,” Aerosp. Sci. Technol. 121, (2022).

[25] M. R. Visbal, “Numerical investigation of deep dynamic stall of a plunging airfoil,” AIAA J. 49, 2152–2170, (2011).

[26] U. Piomelli, J. R. Chasnov, “Theory and applications: Large-eddy simulations,” Turbulence and Transitioning Modelling 2, (1996).

[27] Y. S. Baik, J. M. Rausch, L. P. Bernal, and M. V. Ol, “Experimental investigation of pitching and plunging airfoils at Reynolds number between 1×10^4 and 6×10^4,” in AIAA 39th Fluid Dynamics Conference (2009).

[28] S. B. Pope, “Ten questions concerning the large-eddy simulation of turbulent flows,” New J. Phys. 6, (2004).

[29] J. Jeong, F. Hussain, “On the identification of a vortex,” J. Fluid Mech. 285, 66-94, (1995).